

1           **Climatological Characteristics of Raindrop Size**  
2                           **Distributions in Busan, Korea**

3   Sung-Ho SUH<sup>1</sup>

4  
5   Cheol-Hwan YOU<sup>2\*</sup>

6   Email: [youch@pknu.ac.kr](mailto:youch@pknu.ac.kr)

7  
8   Dong-In LEE<sup>1,2</sup>

9  
10  
11   Institutional addresses:

12   <sup>1</sup> Department of Environmental Atmospheric Sciences, Pukyong National University, Daeyeon  
13   campus 45, Yongso-ro, Namgu, Busan 608-737 Republic of Korea

14  
15   <sup>2</sup>Atmospheric Environmental Research Institute, Daeyeon campus 45, Yongso-ro, Namgu,  
16   Busan 608-737 Republic of Korea

17  
18   \* Corresponding author

20 **Abstract**

21 Raindrop size distribution (DSD) characteristics within the complex area of Busan, Korea  
22 (35.12°N, 129.10°E) were studied using a Precipitation Occurrence Sensor System (POSS)  
23 disdrometer over a four-year period from 24 February 2001 to 24 December 2004. Also, to find  
24 the dominant characteristics of polarized radar parameters which is differential radar  
25 reflectivity ( $Z_{dr}$ ), specific differential phase ( $K_{dp}$ ) and specific attenuation ( $A_h$ ), T-matrix  
26 scattering simulation was applied in present study. To analyze the climatological DSD  
27 characteristics in more detail, the entire period of recorded rainfall was divided into 10  
28 categories not only covering different temporal and spatial scales, but also different rainfall  
29 types. When only convective rainfall was considered, mean values of mass weighted mean  
30 diameter ( $D_m$ ) and normalized number concentration ( $N_w$ ) values for all these categories  
31 converged around a maritime cluster, except for rainfall associated with Typhoons. The  
32 convective rainfall of a Typhoon showed much smaller  $D_m$  and larger  $N_w$  compared with  
33 the other rainfall categories.

34 In terms of diurnal DSD variability, we analyzed maritime (continental) precipitation during  
35 the daytime (DT) (nighttime, NT), which likely results from sea (land) wind identified through  
36 wind direction analysis. These features also appeared in the seasonal diurnal distribution. The  
37 DT and NT Probability Density Function (PDF) during the Summer was similar to the PDF of  
38 the entire study period. However, the DT and NT PDF during the Winter season displayed an  
39 inverse distribution due to seasonal differences in wind direction.

40

41 **Keyword:** DSD, POSS disdrometer, Climatological characteristics, Land and sea wind.

## 42 1. Introduction

43 Raindrop Size Distribution (DSD) is controlled by the microphysical processes of rainfall and  
44 therefore it plays an important role in development of the Quantitative Precipitation Estimation  
45 (QPE) algorithms based on forward scattering simulations of radar measurements (Seliga and  
46 Bringi, 1976). DSD data accurately reflects local rainfall characteristics within an observation  
47 area (You et al., 2014). Many DSD models have been developed to characterize spatial-  
48 temporal differences in DSDs under various atmospheric conditions (Ulbrich, 1983). Marshall  
49 and Palmer (1948) developed an exponential DSD model using DSD data collected by a filter  
50 paper technique ( $N(D) = 8 \times 10^3 \exp(-410R^{-0.21}D)$  in  $m^{-3}mm^{-1}$ ,  
51  $D$  in  $mm$  and  $R$  in  $mm h^{-1}$ ). In subsequent studies, a lognormal distribution was assumed to  
52 overcome the problem of exponential DSD mismatching with real data (Mueller, 1966; Levin,  
53 1971; Markowitz, 1976; Feingold and Levin, 1986).

54 To further investigate natural DSD variations, Ulbrich (1983) developed a gamma DSD that  
55 permitted changing the dimension of the intercept parameter ( $N_0$  in  $m^{-3} mm^{-1-\mu}$ ) with  
56  $N(D) = N_0 D^\mu \exp(-\Lambda D)$ . In addition, to enable the quantitative analysis of different rainfall  
57 events, the development of a normalized gamma DSD model that accounted for the  
58 independent distribution of DSD from the disdrometer channel interval enabled a better  
59 representation of the actual DSD (Willis, 1984; Dou et al., 1999; Testud et al., 2001).

60 DSDs depend on the rainfall type, geographical and atmospheric conditions and observation  
61 time. Also these are closely linked to microphysical characteristics that control rainfall  
62 development mechanisms. In the case of stratiform rainfall, raindrops grow by the accretion  
63 mechanism because of the relatively long residence time in weak updraft condition, in which  
64 almost all water droplets are changed to ice particles. With time, the ice particles grow

65 sufficiently and fall to the ground. The raindrop size of stratiform rainfall observed at the  
66 ground level is larger than that of convective rainfall for a same rainfall intensity due to the  
67 resistance of the ice particles to break-up mechanisms. In contrast to stratiform rainfall,  
68 convective rainfall raindrops grow by the collision-coalescence mechanism associated with  
69 relatively strong vertical wind speeds and short residence time in the cloud. Fully-grown  
70 raindrops of maritime precipitation are smaller in diameter than those in stratiform rainfall due  
71 to the break-up mechanism in case of same rainfall rate (Mapes and Houze Jr, 1993; Tokay and  
72 Short, 1996). Convective rainfall can be classified into two types based on the origin and  
73 direction of movement. Rainfall systems occurring over ocean and land are referred to as  
74 maritime and continental rainfall, respectively (Göke et al., 2007). Continental rainfall is  
75 related to a cold-rain mechanism whereby raindrops grow in the form of ice particles. In  
76 contrast, maritime rainfall is related to a warm-rain mechanism whereby raindrops grow by the  
77 collision-coalescence mechanism. Therefore, the mass-weighted drop diameter ( $D_m$ ) of  
78 continental rainfall observed on the ground is larger than that of maritime rainfall, and a smaller  
79 normalized intercept parameter ( $N_w$ ) is observed in continental rainfall (Bringi et al., 2003).

80 Specific heat is a major climatological feature that creates differences between DSDs in  
81 maritime and continental regions. These two regions have different thermal capacities and thus  
82 different temperature variations are occurred with time. The surface temperature of the ocean  
83 changes slowly because of the higher thermal capacity compared with land. While the  
84 continental regions which have comparatively lower thermal capacity show greater diurnal  
85 temperature variability. Sea winds generally are occurred in from afternoon to early evening  
86 when the temperature gradient between the sea and land becomes negative, which is opposite  
87 gradient in the daytime (DT). In coastal regions, the land and sea wind effect causes a  
88 pronounced difference between the DT and nighttime (NT) DSD characteristics. Also, when

89 mountains are located near the coast, the difference is intensified by the effect of mountain and  
90 valley winds (Qian, 2008).

91 In the present study, we analyzed a four-year dataset spanning from 2001 to 2004, collected  
92 from Busan, Korea (35.12°N, 129.10°E) using a Precipitation Occurrence Sensor System  
93 (POSS) disdrometer, to investigate the characteristics of DSDs in Busan, Korea which consist  
94 complex mid-latitude region comprising both land and ocean. To quantify the effect of land  
95 and sea wind on these characteristics, we also analyzed diurnal variations in DSDs. The  
96 remainder of the manuscript is organized as follows. In Section 2 we review the normalized  
97 gamma model and explain the DSD quality control method and the classification of rainfall. In  
98 Section 3 we report the results of DSD analysis with respect to stratiform/convective and  
99 continental/maritime rainfall, and discuss diurnal variations. Finally, a summary of the results  
100 and the main conclusions are presented in Section 4.

101

## 102 **2. Data and Methods**

### 103 **2.1. Normalized Gamma DSD**

104 DSDs are defined by  $N(D) = N_0 \exp(-\Lambda D)$  ( $\text{m}^{-3}\text{mm}^{-1}$ ) and are reflect the microphysical  
105 characteristics of rainfall using the number concentration of raindrops ( $N(D)$ ). Also, DSDs are  
106 able to calculate the many kind of parameters which show the dominant feature of raindrops.  
107 Normalization is used to define the DSD and to solve the non-independence of each DSD  
108 parameter (Willis, 1984; Dou et al., 1999; Testud et al., 2001). Furthermore, a normalized  
109 gamma DSD enables the quantitative comparison for rainfall cases regardless of time scale and  
110 rain rate. Here, we use the DSD model designed by Testud et al. (2001):

111

112 
$$N(D) = N_w f(\mu) \left(\frac{D}{D_m}\right)^\mu \exp\left[-(4 + \mu) \frac{D}{D_m}\right]. \quad (1)$$

113

114 where  $D$  is the volume equivalent spherical raindrop diameter (mm), and  $f(\mu)$  is defined

115 using the DSD model shape parameter ( $\mu$ ) and gamma function ( $\Gamma$ ) as follows:

116

117 
$$f(\mu) = \frac{6}{4^4} \frac{(\mu+4)^{4+\mu}}{\Gamma(4+\mu)}. \quad (2)$$

118

119 From the value of  $N(D)$ , the median volume diameter ( $D_0$  in mm) can be obtained as follows:

120

121 
$$\int_0^{D_0} D^3 N(D) dD = \frac{1}{2} \int_0^{D_{\max}} D^3 N(D) dD. \quad (3)$$

122

123 Mass-weighted mean diameter ( $D_m$  in mm) is calculated as the ratio of the fourth to the third

124 moment of the DSD:

125

126 
$$D_m = \frac{\int_0^{D_{\max}} D^4 N(D) dD}{\int_0^{D_{\max}} D^3 N(D) dD}. \quad (4)$$

127

128 The normalized intercept parameter ( $N_w$  in  $m^{-3}mm^{-1}$ ) is calculated as follows:

129

$$130 \quad N_w = \frac{4^4}{\pi \rho_w} \left( \frac{LWC}{D_m^4} \right). \quad (5)$$

131

132 The shape of the DSD is calculated as the ratio of  $D_m$  to the standard deviation (SD) of  $D_m$   
133 ( $\sigma_m$  in mm) (Ulbrich and Atlas, 1998; Bringi et al., 2003; Leinonen et al., 2012):

134

$$135 \quad \sigma_m = \left[ \frac{\int_0^{D_{max}} D^3 (D - D_m)^2 N(D) dD}{\int_0^{D_{max}} D^3 N(D) dD} \right]^{\frac{1}{2}}. \quad (6)$$

136

137 In addition,  $\sigma_m/D_m$  is related to  $\mu$  as follows:

138

$$139 \quad \frac{\sigma_m}{D_m} = \frac{1}{(4 + \mu)^{1/2}}. \quad (7)$$

140

141 Liquid water content (LWC in  $g m^{-3}$ ) can be defined from the estimated DSD:

142

$$143 \quad LWC = \frac{\pi}{6} \rho_w \int_0^{D_{max}} D^3 N(D) dD. \quad (8)$$

144

145 where  $\rho_w$  is the water density ( $\text{g m}^{-3}$ ) and it assumed as  $1 \times 10^6 \text{ g m}^{-3}$  for a liquid. Similarly,  
146 the rainfall rate (R in  $\text{mm h}^{-1}$ ) can be defined as follows:

147

$$148 \quad R = \frac{3.6 \pi}{10^3 \cdot 6} \int_0^{D_{\max}} v(D) D^3 N(D) dD. \quad (9)$$

149

150 where the value of factor  $3.6 \times 10^3$  is the unit conversion which converts the mass flux unit  
151 ( $\text{mg m}^{-2} \text{ s}^{-1}$ ) to the common unit ( $\text{mm h}^{-1}$ ) for the convenience.  $v(D)$  ( $\text{m s}^{-1}$ ) is the  
152 terminal velocity for each raindrop size. The relationship between  $v(D)$  and  $D$  (mm) is given  
153 by Atlas et al. (1973) who developed an empirical formula based on the data reported by Gunn  
154 and Kinzer (1949):

155

$$156 \quad v(D) = 9.65 - 10.3 \exp[-0.6D]. \quad (10)$$

157

## 158 **2.2 Quality Control of POSS Data**

159 POSS is used to measure the number of raindrops within the diameter range of 0.34-5.34  
160 mm, using bistatic, continuous wave X-band Doppler radar (10.525 GHz) across 34 channels  
161 (Fig. 1; Sheppard and Joe, 2008). To estimate DSDs, Doppler power density spectrum is  
162 calculated as follows;

163

164

$$S(f) = \int_{D_{\min}}^{D_{\max}} N(D_m) V(D_m, \rho, h, w) \bar{S}(f, D_m, \rho, h, w) dD_m. \quad (11)$$

166

167 Where  $S(f)$  means Doppler spectrum power density,  $V(D_m, \rho, h, w) \bar{S}(f, D_m, \rho, h, w)$  means  
 168 weighting function of  $S(f)$ ,  $\bar{S}$  is the mean of  $S(f)$ ,  $\rho$  is density of precipitation distribution,  $h$   
 169 is the shape of precipitation distribution,  $w$  ( $\text{m s}^{-1}$ ) is wind speed and  $V(x)$  is sample  
 170 volume and the symbol 'x' means arbitrary parameters which affect the sampling volume. The  
 171 Doppler power density spectrum has a resolution of 16Hz and terminal velocity ( $v_t$ ) has a  
 172 resolution of  $0.24 \text{ m s}^{-1}$ . Transmitter and receiver skewed about  $20^\circ$  toward each other, and  
 173 cross point of signal is located over 34 cm from transmitter-receiver. Transmitter-receiver  
 174 toward upper side detects  $N(D)$  in  $V(x)$  (Sheppard, 1990). Also, Sheppard (1990) and  
 175 Sheppard and Joe (1994) noted some shortcomings as the overestimation of small drops at  
 176 horizontal wind larger than  $6 \text{ m s}^{-1}$ . However, in present study, the quality control of POSS  
 177 for wind effect was not considered because it lies beyond this work. Detailed specifications  
 178 and measurement ranges and raindrop sizes for each observation channel of the POSS  
 179 disdrometer are summarized in Table 1.

180 A POSS disdrometer have been operating in Busan, Korea ( $35.12^\circ\text{N}$ ,  $129.10^\circ\text{E}$ ), along with  
 181 other atmospheric instruments, the locations of which are shown in Fig. 2. Estimating raindrop  
 182 diameter correctly is challenging and care should be taken to ensure reliable data are collected.  
 183 We performed the following quality controls to optimize the accuracy of the disdrometer  
 184 estimates. i) Non-liquid type event data (e.g., snow, hail etc.) detected by POSS were excluded  
 185 by routine observation and surface weather chart provided by Korea Meteorological  
 186 Administration (KMA). ii) DSD spectra in which drops were not found in at least five

187 consecutive channels were removed as non-atmospheric. iii) Only data recorded in more than  
188 10 complete channels were considered. iv) To compensate for the reduced capability to detect  
189 raindrops smaller than 1 mm when  $R > 200 \text{ mm h}^{-1}$  (as recorded by the disdrometer), data  
190 for  $R > 200 \text{ mm h}^{-1}$  were not included in the analyses, even though the number of samples was  
191 only 64 for the entire period. v) To eliminate wind and acoustic noise, data collected when  $R <$   
192  $0.1 \text{ mm h}^{-1}$  are removed (Tokay and Short, 1996).

193 After performing all quality control procedures, 99,388 spectra were left from original data  
194 (166,682) for 1-min temporal resolution. Accumulated rainfall amount from POSS during the  
195 entire period was 4261.49 mm. To verify the reliability of the POSS data, they were compared  
196 with data collected by a 0.5 mm tipping bucket rain gauge at an automatic weather system  
197 (AWS) located ~368 m from the POSS (Fig. 3).

198

### 199 **2.3 Radar Parameters**

200 First, the radar reflectivity factor ( $z$  in  $\text{mm}^6\text{m}^{-3}$ ) and non-polarized radar reflectivity ( $Z$  in  
201 dBZ) were computed using the DSD data collected by POSS, as follows:

202

$$203 \quad z = \int_0^{D_{\max}} D^6 N(D) dD. \quad (12)$$

204

$$205 \quad Z = 10 \log_{10}(z). \quad (13)$$

206

207 The T-matrix method used in this study is initially proposed by Waterman (1965, 1971) to

208 calculate electromagnetic scattering by single non-spherical raindrops. The adaptable  
209 parameters for this calculation are frequency, temperature, hydrometeor types, raindrop's  
210 canting angle and axis ratio ( $\gamma$ ) and explained the following sentences. Axis ratios of raindrops  
211 differ with atmospheric conditions and rainfall type. To derive the drop shape relation from the  
212 drop diameter, we applied the results of numerical simulations and wind tunnel tests employing  
213 a forth-polynomial equation, as in many previous studies (Beard and Chuang, 1987;  
214 Pruppacher and Beard, 1970; Andsager et al., 1999; Brandes et al., 2002). The axis ratio  
215 relation used in the present study is a combination of those from Andsager et al. (1999) and  
216 Beard and Chuang (1987) for three raindrop size ranges (Bringi et al., 2003).  
217 The raindrop axis ratio relation of Andsager et al. (1999) is applied in the range of  $1 <$   
218  $D$  (mm)  $< 4$ , as follows:

219

$$220 \quad r = 1.0048 + 0.0057D - 2.628D^2 + 3.682D^3 - 1.677D^4. \quad (14)$$

221

222 The drop-shape relation of Beard and Chuang (1987) is applied in the range of  $D < 1$  mm  
223 and  $D > 4$  mm, as follows:

224

$$225 \quad r = 1.012 + 0.01445D - 0.01028D^2. \quad (15)$$

226

227 We assumed SD and the mean canting angle of raindrops as  $7^\circ$  and  $0^\circ$ , respectively. The  
228 refractive indices of liquid water at  $20^\circ\text{C}$  were used (Ray, 1972). Also, the condition of

229 frequency for electromagnetic wave of radar is 2.85 GHz (S-band). We calculated dual  
230 polarized radar parameters based on these conditions. The parameters of differential reflectivity  
231 ( $Z_{dr}$  in dB), specific differential phase ( $K_{dp}$  in  $\text{deg km}^{-1}$ ), and attenuation ( $A_h$  in  $\text{dB km}^{-1}$ ),  
232 using DSD data were calculated and analyzed.

233

#### 234 **2.4. Classification of Rainfall Types and Rainfall Events**

235 Rainfall systems can be classified as stratiform or convective in nature, via analysis of the  
236 following microphysical characteristics: i) DSD, using relationships between  $N_0$  and  $R$  ( $N_0 >$   
237  $4 \times 10^9 R^{-4.3}$  in  $\text{m}^{-3}\text{mm}^{-1}$  is considered as convective rainfall, Tokay and Short, 1996;  
238 Testud et al., 2001); ii)  $Z$ , where, according to Gamache and Houze (1982), a rainfall system  
239 that displays radar reflectivity larger than 38 dBZ is considered to be convective; and iii)  $R$ ,  
240 where average value larger than 0.5 mm per 5 min is considered as convective rainfall (Johnson  
241 and Hamilton, 1988). Alternatively, rainfall that has 1-min  $R > 5$  (0.5)  $\text{mm h}^{-1}$  and a SD of  
242  $R > (<) 1.5 \text{ mm h}^{-1}$  is considered as convective (stratiform) type (Bringi et al., 2003). The  
243 rainfall classification method proposed by Bringi et al. (2003) is applied in the present study.  
244 It is necessary to categorize different rainfall systems because their microphysical  
245 characteristics show great variation depending on the type of rainfall, as well as the type of  
246 rainfall event; e.g., Typhoon, Changma, heavy rainfall and seasonally discrete rainfall. To  
247 investigate the temporal variation in DSDs, we analyzed daily and seasonal DSDs. Likewise,  
248 to investigate diurnal variability in DSD, DT and NT data were considered by using the sunrise  
249 and sunset time in Busan (provided by the Korea Astronomy and Space Science Institute  
250 [KASI]). In the middle latitudes, and including Busan, the timings of sunrise and sunset vary  
251 due to solar culminating height. The earliest and latest sunrise (sunset) time of the entire period

252 is 0509 KST (1712 KST) and 0733 KST (1942 KST), respectively. DT (NT) is defined as the  
253 period from the latest sunrise (sunset) time to the earliest sunset (sunrise) time for the unity of  
254 classification of each time group (Table 2).

255 To analyze the predominant characteristics of DSDs for Typhoon rainfall, nine Typhoon events  
256 were selected from throughout the entire study period which is summarized in Table 2.

257 This study utilizes KMA rainfall warning regulations to identify heavy rainfall events. The  
258 KMA issues a warning if the accumulated rain amount is expected to be  $>70$  mm within a 6-  
259 hour period, or  $>110$  mm within a 12-hour period. Rainfall events classified as Changma and  
260 Typhoon were not included in the classification 'heavy rainfall'.

261 Changma is the localized rainfall system or rainy season that is usually present over the Korean  
262 Peninsula between mid-June and mid-July which is similar to the Meiyu (China) or Baiu  
263 (Japan). The selected dates and periods of each rainfall category are summarized in Table 2.

264

### 265 **3. Results**

#### 266 **3.1. DSD and Radar Parameters**

267 Figure 4 shows the Probability Density Function (PDF) and Cumulative Distribution Function  
268 (CDF) of DSDs and radar parameters with respect to the entire, stratiform and convective  
269 rainfall. The PDFs of DSD and radar parameters were calculated using the non-  
270 parameterization kernel estimation to identify the dominant distribution of each parameter  
271 recorded in Busan. Non-parameterization kernel estimation was also used to identify  
272 continuous distributions of DSDs. The PDF of stratiform rainfall is more similar to that of the  
273 dataset for the entire analysis period due to the dominant contribution of stratiform rainfall

274 (about 62.93%) to the overall rainfall than that of convective rainfall. However, the PDF for  
275 convective rainfall is significantly different from that of the entire analysis period, and as the  
276 convective rainfall contributes only 6.11% of the overall rainfall (Table 3). When  $\mu < 0$  the  
277 distribution of  $\mu$  for convective rain has more value of PDF than that for stratiform rain (Fig.  
278 4a). Alternatively, the frequency of  $\mu$  for stratiform rainfall is higher than that of convective  
279 rainfall when  $0 < \mu < 5$ . The value of  $\mu$  for convective rainfall is higher than that for  
280 stratiform rainfall because the break-up mechanism would be increase the number  
281 concentration of small raindrops. The number concentrations of mid-size raindrops increased  
282 due to the decrease in the number concentration of relatively large raindrops (Hu and Srivastava,  
283 1995; Sauvageot and Lacaux, 1995). However, we observed a higher frequency of convective  
284 rainfall than stratiform rainfall in the negative  $\mu$  range.

285 The PDF of  $D_m$  displays peak around 1.2 and 1.4 mm for stratiform rainfall and the entire  
286 rainfall dataset, respectively. We note that a gentle peak exists around 0.7 mm for both  
287 stratiform and convective rainfall datasets (Fig. 4b). These features are similar to the  
288 distribution of  $D_m$  observed in a high-latitude region at Järvenpää, Finland (Fig. 4 of Leinonen  
289 et al., 2012). For  $D_m$  values  $> 1.7$  mm, the PDF for convective rainfall is higher than  
290 stratiform rainfall. Accordingly, the value of DSD for stratiform rainfall is higher than that of  
291 convective rainfall when  $D_m < 1.7$  mm. Generally, stratiform rainfall that develops by the  
292 cold rain process displays weaker upward winds and less efficient break-up of raindrops.  
293 Therefore, in the same rainfall rate, stratiform rainfall tends to produce larger raindrops than  
294 convective rainfall that develops by the warm rain process. However, the average  $D_m$  values  
295 for convective and stratiform rain for the entire period are approximately 1.45 and 1.7 mm,

296 respectively. In short,  $D_m$  is proportional to  $R$  regardless of rainfall type. This finding is  
297 consistent with the results of Atlas et al. (1999) who found that the  $D_m$  of convective rainfall  
298 is larger than that of stratiform rainfall on Kapingamarangi Island, Micronesia.

299 The PDF of  $\log_{10}(N_w)$  for the entire rainfall dataset was evenly distributed between 1.5 and  
300 5.5, with a peak at  $N_w = 3.3$  (Fig. 4c). The PDF of  $\log_{10}(N_w)$  for stratiform rainfall is rarely  
301  $> 5.5$ , while for convective rainfall it is higher at  $> 5.5$  than that of stratiform. There is a similar  
302 frequency in the stratiform and convective rainfall at 4.4.

303 The PDF distributions for  $\log_{10}(R)$  and  $\log_{10}(LWC)$  are similar each other (Fig. 4d and e).  
304 It is inferred that the similar results come from the using of alike moment of DSD as 3.67 and  
305 3 for  $R$  and  $LWC$ , respectively. The PDF of  $\log_{10}(R)$  for the entire rainfall dataset ranged  
306 between -0.5 and 2. A peak exists at 0.3 and the PDF rapidly decreases from the peak value as  
307  $R$  increases. The PDF for stratiform rainfall has a higher frequency than that of the entire  
308 rainfall when  $-0.3 < \log_{10}(R) < 0.7$ , while the PDF for convective rainfall is denser between  
309 0.4 and 2. Furthermore, the frequency of the PDF for convective rainfall was higher than that  
310 of stratiform rainfall in case of  $\log_{10}(R) > 0.65$  and the peak value shown as 0.9.

311 The PDF and CDF for  $Z$ ,  $Z_{dr}$ ,  $K_{dp}$  and  $A_h$  are shown in Fig. 4f-i. The PDF of  $Z$  for  
312 stratiform rainfall (Fig. 4f) is widely distributed between 10 and 50 dBZ with the peak at  
313 approximately 27 dBZ. Conversely, for convective rainfall, the value of PDF lie between 27  
314 and 55 dBZ and the peak frequency value at approximately 41 dBZ. The frequency value of  
315 reflectivity is higher for convective rainfall than for stratiform rainfall in the range of  $\sim >35$   
316 dBZ. Furthermore, the shape of the PDF for convective rainfall is similar to that reported for  
317 Darwin, Australia (Steiner et al., 1995); however, for stratiform rainfall there are significant  
318 differences between Busan and Darwin in terms of the shape of the frequency distribution. The

319 PDF of  $Z_{dr}$  for the entire rainfall primarily exists between 0 and 2.5 dB, and the peaks are at  
320 0.3 and 1.8 dB (Fig. 4g). The distribution of  $Z_{dr}$  for convective and stratiform rainfall is  
321 concentrated between 0.6 and 1.6 dB, and between 0.3 and 2 dB, respectively. The frequency  
322 of  $Z_{dr}$  for convective (stratiform) rainfall exists in ranges higher (lower) than stratiform  
323 (convective) at 0.9 dB.

324 The dominant distribution of  $K_{dp}$  for the entire dataset and for stratiform rainfall lies  
325 between 0 and 0.14  $\text{deg km}^{-1}$ , with a peak value of 0.03  $\text{deg km}^{-1}$  and 0.08  $\text{deg km}^{-1}$ .  
326 However, for convective rainfall the PDF of  $K_{dp}$  is evenly exist between 0.01 and 0.15  
327  $\text{deg km}^{-1}$ . Furthermore, when  $K_{dp} > 0.056 \text{ deg km}^{-1}$ , the frequency of the PDF for  
328 convective rainfall is higher than that of stratiform rainfall (Fig. 4h).

329 The PDF of  $A_h$  is similar to that of  $K_{dp}$  and is exist between 0 and 0.01  $\text{dB km}^{-1}$ . For the  
330 case of the entire rainfall dataset and for stratiform rainfall, the PDF of  $A_h$  is concentrated  
331 between 0 and  $2.0 \times 10^{-3} \text{ dB km}^{-1}$  and that of convective rainfall is strongly concentrated  
332 between  $1.0 \times 10^{-3}$  and  $8.0 \times 10^{-3} \text{ dB km}^{-1}$  (Fig. 4i). Unlike the PDF of  $A_h$  for  
333 convective rainfall, the PDF for stratiform rainfall shows a strong peak at about  $7.0 \times 10^{-4}$   
334  $\text{dB km}^{-1}$ .

335

### 336 **3.2. Climatological Characteristics of DSD in Busan**

337 The climatological characteristics of DSDs for 10 rainfall categories are analyzed in this study.  
338 Sample size and ratio rainfall for each category are summarized in Table 3. Figure 5a illustrates  
339 the distribution of all 1-min stratiform rainfall data, and Fig. 5b shows scatter plots of averaged  
340  $D_m$  and  $\log_{10}(N_w)$  for all 10 rainfall categories for stratiform rainfall data. Figure 5a displays  
341 a remarkable clear boundary in the bottom sector and shows that most of the data lie below the

342 reference line used by Bringi et al. (2003) to classify convective and stratiform rainfall. The  
343 average value of  $D_m$  and  $\log_{10}(N_w)$  for all rainfall categories, except for heavy rainfall,  
344 exist between 1.4 mm and 1.6 mm and between 3.15 and 3.5, respectively (Fig. 5b). These  
345 values are relatively small compared with the reference line presented by Bringi et al. (2003).  
346 The distribution of 1-min convective rainfall data is displayed in Fig. 6a and the distribution of  
347 average values of  $D_m$  and  $N_w$  for the 10 rainfall categories in the case of convective rainfall  
348 in Fig. 6b. The blue and red plus symbols represent maritime and continental rainfall,  
349 respectively, as defined by Bringi et al. (2003). The scatter plot of 1-min convective rainfall  
350 data shows more in the continental cluster than the maritime cluster; however, the average  
351 values for the 10 rainfall categories are all located around the maritime cluster, except for the  
352 Typhoon category. By considering the entire average values including Typhoon event (Fig. 6b),  
353 we can induce the simple linear equation using  $D_m$  and  $\log_{10}(N_w)$  as follows:

354

$$355 \log_{10}(N_w) = -1.8D_m + 6.9. \quad (16)$$

356

357 Even the coefficients in Eq. 16 might be changed slightly with the Typhoon values, this result  
358 does not represent in  $D_m < 1.2$  mm and  $D_m > 1.9$  mm. The  $D_m$  ( $N_w$ ) value for the Typhoon  
359 category was considerably smaller (larger) than that of the other categories as well as that of  
360 stratiform type of Typhoon. This result does not agree with that reported by Chang et al. (2009),  
361 who noted that the  $D_m$  of convective rainfall Typhoon showed a large value compared with  
362 that associated with stratiform rainfall.

363

### 364 **3.3 Diurnal Variation in Raindrop Size Distributions**

#### 365 **3.3.1. Diurnal Variations in DSDs**

366 Figure 7a shows a histogram of normalized frequency of 16 wind directions recorded by the  
367 AWS, which is the same instrument as that used to collect the data shown in Fig. 3. To establish  
368 the existence of a land and sea wind, the difference in wind direction frequencies between DT  
369 and NT were analyzed. Figure 7b shows the difference between DT and NT, difference  
370 frequency means normalized frequency of wind direction for DT subtract to that of NT for each  
371 direction, in terms of the normalized frequency of 16 wind directions. In other word, positive  
372 (negative) values indicate that the frequency of wind is more often observed during DT (NT).  
373 Also, land (sea) wind defined in present study from  $225^\circ$  ( $45^\circ$ ) to  $45^\circ$  ( $225^\circ$ ) according to the  
374 geographical condition in Busan. The predominant frequency of wind direction in the DT (NT),  
375 between  $205^\circ$  ( $22.5^\circ$ ) and  $22.5^\circ$  ( $205.5^\circ$ ), is higher than that in the NT (DT) (Fig. 7b). The  
376 observation site where the POSS was installed at western side from the closest coast line,  
377 distance is about 611 m, suggesting that the effect of the land and sea wind would have been  
378 recorded. To understand the effects of the land and sea wind on DSD characteristics, we  
379 analyzed the PDF and 2-hour averaged DSD parameters for DT and NT. Figure 8 illustrates the  
380 distributions of  $\mu$ ,  $D_m$ ,  $\log_{10}(N_w)$ ,  $\log_{10}(LWC)$ ,  $\log_{10}(R)$ , and  $Z$ . There were large  
381 variations of  $\mu$  with time. The  $\mu$  values varied from 2.41 to 3.17 and the minimum and  
382 maximum  $\mu$  values occurred at 08:00 KST and 12:00 KST, respectively (Fig. 8a). A  $D_m$   
383 larger than 1.3 mm dominated from 00:00 KST to 12:00 KST, before decreasing remarkably  
384 between 12:00 and 14:00 KST. The minimum and maximum  $D_m$  appeared at 14:00 KST and  
385 08:00 KST, respectively (Fig. 8b).

386  $N_w$  distribution showed inversely to  $D_m$ ; however, no inverse relationship was identified  
387 between  $D_m$  and  $N_w$  in case of the time series (Fig. 8c). The maximum and minimum values  
388 of  $N_w$  were found at 06:00 KST and 22:00 KST.

389 Variability through time was similar for  $R$ ,  $LWC$ , and  $Z_h$  as  $D_m$ . There was an increasing  
390 trend from 00:00 KST to 08:00 KST followed by a remarkably decreasing trend from 08:00  
391 KST to 14:00 KST (Figs 8d, 11e and 11f). Note that the time of the sharp decline for  $R$   
392 between 12:00 KST and 14:00 KST is simultaneous with a  $D_m$  decrease. Larger (smaller)  
393 drops would contribute to higher  $R$  in the morning (afternoon). These variations considerably  
394 matched with the diurnal sea wind time series (Fig. 8g). Sea wind is the sum value of  
395 normalized wind frequency between  $45^\circ$  and  $225^\circ$ . From 02:00 (14:00) KST to 12:00 (20:00)  
396 KST shows smaller (larger) value of sea wind frequency which is opposite to the relatively  
397 larger (smaller) parts of each parameter ( $D_m$ ,  $R$ ,  $LWC$  and  $Z_h$ ).

398 The PDF distribution of  $\mu$  between -2 and 0 is more concentrated for NT than for DT.  
399 Furthermore, when  $\mu > 0$ , DT and NT frequency distributions are similar (Fig. 9a). A larger  
400  $N(D)$  of small or large raindrops would be expected in NT than in DT.

401 The distribution of DT  $D_m < 0.7 \text{ mm}$  is wider than that of the NT. However, between 0.7  
402 and 1.5  $\text{mm}$  the frequency for NT is higher than that for DT, whereas the distribution in the  
403 range  $D_m > 1.5 \text{ mm}$  is similar for both DT and NT (Fig. 9b). We note that the smaller peak  
404 of  $D_m$  around 0.6  $\text{mm}$  for the entire rainfall dataset (Fig. 4b) was observed only in DT.

405 The distribution of  $\log_{10}(N_w)$  for DT has higher value of PDF at larger  $\log_{10}(N_w)$  than that  
406 of NT at  $\log_{10}(N_w) > 4$  (Fig. 9c).

407 Bringi et al. (2003) noted that the maritime climatology displayed larger  $N_w$  and smaller  $D_m$   
408 values than the continental climatology, based on observed DSDs in the low and middle latitude.

409 Also, Göke et al. (2007) emphasized that rainfall type can be defined by the origin location and  
410 movement direction. In accordance with these previous results, we consider NT rainfall in the  
411 Busan region to be more likely caused by a continental convective system.

412 In the present study, the shape of the PDF of  $LWC$  and  $R$  for DT and NT are similar which is  
413 the same reason with the results of Fig. 4e-f.  $LWC$  and  $R$  distributions during the DT (NT)  
414 are higher (lower) than in the NT (DT) when  $\log_{10}(LWC)$  and  $\log_{10}(R)$  are larger (smaller)  
415 than -1.2 and 0, respectively (Fig. 9d and e).  $Z$  has similar pattern with  $LWC$  and  $R$  during  
416 the DT (NT) was higher (lower) than in the NT (DT) in the range below (above) about 27  $dBZ$   
417 (Fig. 9f).

418

### 419 **3.3.2. Diurnal Variations of DSDs with respect to Season**

420 Busan experiences distinct atmospheric conditions that are caused by the different frequencies  
421 and magnitudes of land and sea winds in response to variable sunrise and sunset times. To  
422 identify seasonal variations of DSDs with respect to the effect of the land and sea wind, we  
423 analyzed the DT and NT PDF of  $D_m$  and  $N_w$  in the Summer and Winter. The start and end  
424 times of DT (NT) were sorted using the latest sunrise (sunset) and the earliest sunset (sunrise)  
425 time for each season (Table 4) which is same method that of entire period classification.

426 Figure 10a shows a histogram of wind directions in Summer (light grey) and Winter (dark grey).

427 The frequencies of Summer and Winter wind directions are similar to each other. However, in  
428 Fig. 10b, the DT and NT distributions of Winter wind direction display opposing frequencies.

429 Note that Winter season shows remarkable frequency of land (sea) wind between  $0^\circ$  ( $157.5^\circ$ )  
430 and  $45^\circ$  ( $202.5^\circ$ ) at DT (NT) compared with results of those for Summer season. The  
431 accumulated value of normalized wind frequencies at the sea and land wind show different

432 feature between Summer and Winter season (Table 5).

433 To identify the variability of DSDs caused by the land and sea wind in Summer and Winter, a  
434 2-hour interval time series of  $D_m$ ,  $N_w$  and  $R$  was analyzed. In the Summer, the time series  
435 of  $D_m$  displays considerably large values between 00:00 KST and 12:00 KST, compared with  
436 the period between 14:00 KST and 22:00 KST (Fig. 11a). The mean value of  $D_m$  decreases  
437 dramatically between 12:00 KST and 14:00 KST.  $\log_{10}(N_w)$  has a negative relationship with  
438  $D_m$  (Fig. 11b). However, the inverse relation between  $\log_{10}(N_w)$  and  $D_m$  is not remarkable.  
439  $\log_{10}(R)$  tends to increase gradually from 00:00 KST to 08:00 KST and decrease from 08:00  
440 KST to 14:00 KST, which is similar to the pattern that of entire period (Fig. 11c). Kozu et al.  
441 (2006) analyzed the diurnal variation in  $R$  at Gadanki (South India), Singapore, and  
442 Kototabang (West Sumatra) during the Summer monsoon season. All regions displayed  
443 maximum  $R$  at approximately 16:00 LST, except for Gadanki. Also, Qian (2008), who analyzed  
444 the diurnal variability of wind direction and  $R$  on Java Island during the Summer season using  
445 30 years (from 1971 to 2000) of NCEP/NCAR reanalyzed data. They found that a land wind  
446 occurred from 01:00 LST to 10:00 LST and a sea wind from 13:00 LST to 22:00 LST (Fig. 7  
447 of Qian (2008)). Normalized wind frequency for each direction is similar pattern to the results  
448 of Qian (2008) but pattern of  $R$  is different with that of Kozu et al. (2006). The diurnal variation  
449 of rain rate in the present study from 02:00 (12:00) KST to 10:00 (20:00) KST shows relatively  
450 smaller (larger) frequencies of sea wind. It is different pattern with the result of Kozu et al.  
451 (2006). However, these patterns matched with the time series of  $D_m$  and  $\log_{10}(N_w)$ . Larger  
452 frequency of sea wind direction shows counter-proportional (proportional) relationship to the  
453 smaller (larger) frequency of  $D_m$  ( $\log_{10}(N_w)$ ).

454 Variability of  $D_m$  time series for Winter is the inverse of the Summer time series (Fig. 11a).

455 The mean value of  $D_m$  steadily increases from 00:00 KST to 16:00 KST and then decreases  
 456 from 16:00 KST to 22:00 KST. The Winter  $\log_{10}(N_w)$  time series displays a clear inverse  
 457 pattern compared with the  $D_m$  variation with time and increases from 1600 KST to 0400 KST  
 458 and then steadily decreases from 04:00 KST to 16:00 KST (Fig. 11b). The peak of  $\log_{10}(N_w)$   
 459 occurs at 04:00 KST. However, the time series of  $\log_{10}(R)$  for Winter season shows similar  
 460 pattern with that of Summer unlike to another parameters (Fig. 11c). Based on the diurnal  
 461 variation of  $R$ , the variations of  $D_m$  and  $N_w$  would be independent to  $R$ .  
 462 Alike to the  $D_m$  and  $\log_{10}(N_w)$ , normalized wind frequency of wind direction for Winter  
 463 season shows inverse relationship to that of Summer season (Fig. 11d). The value of frequency  
 464 generally decreases (increases) from 04:00 (14:00) KST to 14:00 (04:00) KST. Also, it shows  
 465 symmetry pattern with that of Summer season.  
 466 The PDF distribution of Summer  $D_m$  displays a relatively large DT frequency compared with  
 467 NT when  $D_m < 1.65 \text{ mm}$ , except for the range between 0.6 and 0.9  $\text{mm}$ . However, in the  
 468 range of  $D_m > 1.65 \text{ mm}$ , the NT PDF displays a larger frequency (Fig. 12a). The PDF of  
 469  $\log_{10}(N_w)$  for DT (NT) has a larger frequency than the NT (DT) when  $\log_{10}(N_w) > (<) 3.3$   
 470 but smaller frequency when  $\log_{10}(N_w) < (>) 3.3$  (Fig. 12c).  
 471 The DT and NT PDFs of  $D_m$  and  $\log_{10}(N_w)$  during Winter display an inverse distribution  
 472 to that of Summer. For the PDF of  $D_m$ , there is a considerable frequency for NT (DT) when  
 473  $D_m < (>) 1.6 \text{ mm}$  (Fig. 12b). The PDF of  $\log_{10}(N_w)$  of Summer season for NT (DT) is  
 474 larger than that of the DT when  $\log_{10}(N_w) < (>) 3.5$  (Fig. 12d). In the PDF analysis, relatively  
 475 large (small)  $D_m$  and small (large)  $\log_{10}(N_w)$  are displayed during the NT (DT) when a land  
 476 wind (sea wind) occurs.  
 477 Bringi et al. (2003) referred that the convective rainfall type is able to be classified as the

478 continental and maritime-like precipitation using  $D_m$  and  $N_w$ . As the previous study result, we  
479 analyzed the PDF of DSDs for Summer and Winter with respect to convective rainfall type.  
480 These feature would be shown more clearly in convective type. The convective rainfall type of  
481 PDFs of DT and NT for Summer show similar shape of distribution to that of all rainfall type  
482 (Fig. 3a). For the PDF of  $D_m$ , there is a more frequency for DT (NT) than NT (DT) when  $D_m$   
483  $< (>) 2.0 \text{ mm}$  except for between  $0.7 \text{ mm}$  and  $1.2 \text{ mm}$  (Fig. 13a). The PDF of convective  
484 rainfall type's  $\log_{10}(N_w)$  for DT (NT) has a larger frequency than the NT (DT) when  
485  $\log_{10}(N_w) > (<) 3.4$  except for between 4.3 and 5.5 (Fig. 12c). PDF distributions for Winter  
486 season show more clear pattern compared with those of the entire rainfall type. The value of  
487 PDF for  $D_m$  in DT (NT) have considerably larger than NT (DT) when  $D_m > (<) 1.9 \text{ mm}$ ,  
488 especially between  $2.15 \text{ mm}$  and  $2.3 \text{ mm}$  (Fig. 13b). Also, those for  $\log_{10}(N_w)$  in DT (NT)  
489 show dramatic values when  $\log_{10}(N_w) < (>) 3.6$ . Furthermore, PDF values significantly  
490 concentrated on between  $3 < \log_{10}(N_w) < 3.2$  (Fig. 13d). In short, considering the DSD  
491 parameters with wind directions, the maritime (continental)-like precipitation would depend  
492 on the sea (land) wind.

493

#### 494 **4. Summary and Conclusion**

495 Climatological characteristics of DSDs in Busan were analyzed using the DSD data observed  
496 by POSS over a four-year period from 24 February 2001 to 24 December 2004. Observed DSDs  
497 were filtered to remove errors by performing several quality control measures, and an AWS  
498 rain gauge installed nearby was used to verify the rainfall amount recorded by the POSS. We  
499 analyzed DSD characteristics of convective and stratiform rainfall types, as defined by Bringi  
500 et al. (2003). The rainfall dataset was thus divided into stratiform and convective rainfall and

501 their contributions to the total rainfall were 62.93% and 6.11%, respectively. Also, to find the  
502 climatological characteristics of DSD for rainfall case, the entire rainfall data was classified as  
503 10 rainfall categories including the entire period case.

504 According to the study by Bringi et al. (2003), the rainfall in Busan shows maritime  
505 climatological DSD characteristics. The mean values of  $D_m$  and  $N_w$  for stratiform rainfall are  
506 relatively small compared with the average line of stratiform rainfall produced by Bringi et al.  
507 (2003), except for heavy rainfall events. In case of convective type, mean values of  $D_m$  and  $N_w$   
508 are converged around the maritime cluster, except for the Typhoon category. The convective  
509 rainfall associated with a Typhoon has considerably smaller  $D_m$  and larger  $N_w$  values  
510 compared with the other rainfall categories. This is likely caused by increased raindrop break-  
511 up mechanism as a result of strong wind effects. Furthermore, the distributions of mean  $D_m$   
512 and  $N_w$  values for all rainfall categories associated with convective rainfall displays a linear  
513 relationship including the Typhoon category.

514 The analysis of diurnal variation in DSD yielded the following results: first, the frequency of  
515  $\mu$  is higher at NT than during the DT in the negative value. The PDF of R is higher at NT than  
516 during the DT when  $\log_{10}(R) > 0.6$ . The value of PDF for  $D_m$  during DT is larger than NT  
517 smaller than 0.65 mm. For  $N_w$ , which tends to be inversely related to  $D_m$ , its frequency is higher  
518 at NT than DT when  $\log_{10}(N_w) > 3.8$ . This feature is matched with the time series of normalized  
519 frequency of sea wind which shows inverse relationship to  $D_m$ . Smaller  $D_m$  corresponds to  
520 the larger sea wind frequency. In short, maritime (continental) –like precipitation are observed  
521 in the DT (NT) more often than in the NT (DT) according to the features of wind. The above-  
522 mentioned DSD characteristics are likely due to the land and sea wind caused by differences  
523 in specific heat between the land and ocean. These features are also apparent in the seasonal  
524 diurnal distribution. The PDF of DT and NT for convective rainfall type during the Summer is

525 similar to the PDF of the entire period; however, those of the Winter displays the significant  
526 inverse distribution compared to the Summer because of obvious seasonal differences in wind  
527 direction.

528

529

530

531

532

533

534

535

536

537

538

539

540

541

542

543

544 **Author contributions**

545 Cheol-Hwan You designed the study. Sung-Ho Suh modified the original study theme and  
546 performed the study. Cheol-Hwan You and Sung-Ho Suh performed research, obtained the  
547 results and prepared the manuscript along with contributions from all of the co-authors. Dong-  
548 In Lee examined the results and checked the manuscript.

549

550 **Acknowledgement**

551 This work was funded by the Korea Meteorological Industry Promotion Agency under Grant  
552 KMIPA 2015-1050. The authors acknowledge providing, weather chart, and AWS data for this  
553 work from the Korea Meteorological Administration and codes for scattering simulation from  
554 Professor V. N. Bringi at Colorado State University.

555

556

557

558

559

560

561

562

563

564 **References**

- 565 Andsager, K., Beard, K. V., and Laird, N. F.: Laboratory measurements of axis ratios for large  
566 raindrops, *Journal of the Atmospheric Sciences*, 56, 2673-2683, 1999.
- 567 Atlas, D., Srivastava, R., and Sekhon, R. S.: Doppler radar characteristics of precipitation at  
568 vertical incidence, *Reviews of Geophysics*, 11, 1-35, 1973.
- 569 Atlas, D., Ulbrich, C. W., Marks, F. D., Amitai, E., and Williams, C. R.: Systematic variation  
570 of drop size and radar-rainfall relations, *Journal of Geophysical Research: Atmospheres* (1984–  
571 2012), 104, 6155-6169, 1999.
- 572 Beard, K. V., and Chuang, C.: A new model for the equilibrium shape of raindrops, *Journal of*  
573 *the Atmospheric sciences*, 44, 1509-1524, 1987.
- 574 Brandes, E. A., Zhang, G., and Vivekanandan, J.: Experiments in rainfall estimation with a  
575 polarimetric radar in a subtropical environment, *Journal of Applied Meteorology*, 41, 674-685,  
576 2002.
- 577 Bringi, V., Chandrasekar, V., Hubbert, J., Gorgucci, E., Randeu, W., and Schoenhuber, M.:  
578 Raindrop size distribution in different climatic regimes from disdrometer and dual-polarized  
579 radar analysis, *Journal of the atmospheric sciences*, 60, 354-365, 2003.
- 580 Chang, W.-Y., Wang, T.-C. C., and Lin, P.-L.: Characteristics of the raindrop size distribution  
581 and drop shape relation in Typhoon systems in the western Pacific from the 2D video  
582 disdrometer and NCU C-band polarimetric radar, *Journal of Atmospheric and Oceanic*  
583 *Technology*, 26, 1973-1993, 2009.
- 584 Dou, X., Testud, J., Amayenc, P., and Black, R.: The parameterization of rain for a weather  
585 radar, *Comptes Rendus de l'Académie des Sciences-Series IIA-Earth and Planetary Science*,  
586 328, 577-582, 1999.

587 Feingold, G., and Levin, Z.: The lognormal fit to raindrop spectra from frontal convective  
588 clouds in Israel, *Journal of Climate and Applied Meteorology*, 25, 1346-1363, 1986.

589 Gamache, J. F., and Houze Jr, R. A.: Mesoscale air motions associated with a tropical squall  
590 line, *Monthly Weather Review*, 110, 118-135, 1982.

591 Göke, S., Ochs III, H. T., and Rauber, R. M.: Radar analysis of precipitation initiation in  
592 maritime versus continental clouds near the Florida coast: Inferences concerning the role of  
593 CCN and giant nuclei, *Journal of the Atmospheric Sciences*, 64, 3695-3707, 2007.

594 Gunn, R., and Kinzer, G. D.: The terminal velocity of fall for water droplets in stagnant air,  
595 *Journal of Meteorology*, 6, 243-248, 1949.

596 Hu, Z., and Srivastava, R.: Evolution of raindrop size distribution by coalescence, breakup, and  
597 evaporation: Theory and observations, *Journal of the atmospheric sciences*, 52, 1761-1783,  
598 1995.

599 Johnson, R. H., and Hamilton, P. J.: The relationship of surface pressure features to the  
600 precipitation and airflow structure of an intense midlatitude squall line, *Monthly Weather*  
601 *Review*, 116, 1444-1473, 1988.

602 Kozu, T., Reddy, K. K., Mori, S., Thurai, M., Ong, J. T., Rao, D. N., and Shimomai, T.: Seasonal  
603 and diurnal variations of raindrop size distribution in Asian monsoon region, *JOURNAL-*  
604 *METEOROLOGICAL SOCIETY OF JAPAN SERIES 2*, 84, 195, 2006.

605 Leinonen, J., Moisseev, D., Leskinen, M., and Petersen, W. A.: A climatology of disdrometer  
606 measurements of rainfall in Finland over five years with implications for global radar  
607 observations, *Journal of Applied Meteorology and Climatology*, 51, 392-404, 2012.

608 Levin, Z.: Charge separation by splashing of naturally falling raindrops, *Journal of the*  
609 *Atmospheric Sciences*, 28, 543-548, 1971.

610 Mapes, B. E., and Houze Jr, R. A.: Cloud clusters and superclusters over the oceanic warm

611 pool, *Monthly Weather Review*, 121, 1398-1416, 1993.

612 Markowitz, A. H.: Raindrop size distribution expressions, *Journal of Applied Meteorology*, 15,  
613 1029-1031, 1976.

614 Marshall, J. S., and Palmer, W. M. K.: The distribution of raindrops with size, *Journal of*  
615 *meteorology*, 5, 165-166, 1948.

616 Mueller, E. A.: Radar cross sections from drop size spectra, University of Illinois at Urbana-  
617 Champaign, 1966.

618 Pruppacher, H., and Beard, K.: A wind tunnel investigation of the internal circulation and shape  
619 of water drops falling at terminal velocity in air, *Quarterly Journal of the Royal Meteorological*  
620 *Society*, 96, 247-256, 1970.

621 Qian, J.-H.: Why precipitation is mostly concentrated over islands in the Maritime Continent,  
622 *Journal of the Atmospheric Sciences*, 65, 1428-1441, 2008.

623 Ray, P. S.: Broadband complex refractive indices of ice and water, *Applied Optics*, 11, 1836-  
624 1844, 1972.

625 Sauvageot, H., and Lacaux, J.-P.: The shape of averaged drop size distributions, *Journal of the*  
626 *Atmospheric Sciences*, 52, 1070-1083, 1995.

627 Seliga, T., and Bringi, V.: Potential use of radar differential reflectivity measurements at  
628 orthogonal polarizations for measuring precipitation, *Journal of Applied Meteorology*, 15, 69-  
629 76, 1976.

630 Sheppard, B. E.: Measurement of raindrop size distributions using a small Doppler radar. *J.*  
631 *Atmos. Oceanic Technol.*, 7, 255–268, 1990.

632 Sheppard, B. E. and P. I. Joe: Comparison of raindrop size distribution measurements by a  
633 Joss–Waldvogel disdrometer, a PMS 2DG spectrometer and a POSS Doppler radar. *J. Atmos.*  
634 *Oceanic Technol.*, 11, 874–887, 1994.

635 Sheppard, B., and Joe, P.: Performance of the precipitation occurrence sensor system as a  
636 precipitation gauge, *Journal of atmospheric and Oceanic technology*, 25, 196-212, 2008.

637 Steiner, M., Houze Jr, R. A., and Yuter, S. E.: Climatological characterization of three-  
638 dimensional storm structure from operational radar and rain gauge data, *Journal of Applied  
639 Meteorology*, 34, 1978-2007, 1995.

640 Testud, J., Oury, S., Black, R. A., Amayenc, P., and Dou, X.: The concept of “normalized”  
641 distribution to describe raindrop spectra: A tool for cloud physics and cloud remote sensing,  
642 *Journal of Applied Meteorology*, 40, 1118-1140, 2001.

643 Tokay, A., and Short, D. A.: Evidence from tropical raindrop spectra of the origin of rain from  
644 stratiform versus convective clouds, *Journal of applied meteorology*, 35, 355-371, 1996.

645 Ulbrich, C. W.: Natural variations in the analytical form of the raindrop size distribution,  
646 *Journal of Climate and Applied Meteorology*, 22, 1764-1775, 1983.

647 Ulbrich, C. W., and Atlas, D.: Rainfall microphysics and radar properties: Analysis methods  
648 for drop size spectra, *Journal of Applied Meteorology*, 37, 912-923, 1998.

649 Waterman, P.C.: Matrix formulation of electromagnetic scattering. *Proc. IEEE*, 53, 805-812,  
650 1965.

651 Waterman, P.C.: Symmetry, unitarity, and geometry in electromagnetic scattering, *Physical  
652 review D*, 3, 825, 1971.

653 Willis, P. T.: Functional fits to some observed drop size distributions and parameterization of  
654 rain, *Journal of the Atmospheric Sciences*, 41, 1648-1661, 1984.

655 You, C.-H., Lee, D.-I., and Kang, M.-Y.: Rainfall estimation using specific differential phase  
656 for the first operational polarimetric radar in Korea, *Advances in Meteorology*, 2014, 10 pages,  
657 2014.

658

659 **Tables**

660

661 **Tables 1.** Specification of POSS disdrometer.

<b>Specifications</b>	<b>Detail</b>
<b>Manufacturer</b>	ANDREW CANADA INC
<b>Module</b>	PROCESSOR
<b>Model number</b>	POSS-F01
<b>Nominal power</b>	100 mW
<b>Bandwidth</b>	Single frequency
<b>Emission</b>	43 mW
<b>Pointing direction</b>	20 ° (to the vertical side)
<b>Antenna</b>	Rectangular pyramidal horns
<b>Range of sample area</b>	< 2 m
<b>Wavelength</b>	10.525 GHz $\pm$ 15 GHz
<b>Physical dimension</b>	277×200×200 cm <sup>3</sup>
<b>Net weights</b>	Approximately 110 kg

662

663

664

665

666

667

668

669

670

671 **Table 2.** Designated date with respect to the source of rainfall.

Rainfall Category	Period			
	2001	2002	2003	2004
<b>Typhoon</b>	-	5-6 July, 31 August	29 May, 19 June, 7 August, 11-12 September	20 June, 19 August, 6 September
<b>Changma</b>	18-19 June, 23-26 June, 29-30 June, 1 July, 5-6 July, 11-14 July	23-25 June, 30 June, 1-2 July	12-14 June, 23 June, 27 June, 30 June, 1 July, 3-15 July	11-14 July
<b>Heavy rainfall</b>	15 April 2002, 20:13 KST to 16 April 2002, 06:29 KST			
<b>Seasonal</b>	<b>Spring</b>	<b>Summer</b>	<b>Autumn</b>	<b>Winter</b>
	March to May	June to August	September to November	December to February
<b>Diurnal</b>	<b>DT (KST)</b>		<b>NT (KST)</b>	
	07:33-17:12		19:42-05:09	

673

674

675

676

677

678

679

680

681

682 **Table 3.** Rainfall rate for each rainfall category and the number of sample size for 1-min data.

<b>Rainfall Category</b>	<b>Total precipitation</b>	<b>Stratiform precipitation (%)</b>	<b>Convective precipitation (%)</b>
<b>Typhoon</b>	5095	3118 (61.19)	652 (12.79)
<b>Changma</b>	18526	11099 (59.91)	1611 (8.69)
<b>Heavy rainfall</b>	359	153 (42.61)	150 (41.78)
<b>Spring</b>	30703	20370 (66.34)	1478 (4.81)
<b>Summer</b>	37187	22566 (60.68)	3409 (9.16)
<b>Autumn</b>	19809	12033 (60.74)	850 (4.29)
<b>Winter</b>	11689	7582 (64.86)	339 (2.90)
<b>Daytime</b>	41328	26373 (63.81)	2539 (6.14)
<b>Nighttime</b>	37455	23063 (84.00)	2242 (5.89)
<b>Entire</b>	99388	62551 (62.93)	6076 (6.11)

683

684

685

686

687 **Table 4.** DT and NT (KST) in Summer and Winter season.

<b>Rainfall Category</b>	<b>Period</b>	<b>Beginning time (KST)</b>	<b>Finishing time (KST)</b>
<b>Summer</b>	<b>DT</b>	05:33	19:27
	<b>NT</b>	19:42	05:09
<b>Winter</b>	<b>DT</b>	07:33	17:12
	<b>NT</b>	18:19	06:54

688

689

690

691

692

693

694

695

696

697

698

699

700

701

702 **Table 5.** Sum of the normalized wind direction frequencies between Summer and Winter.

Sum of the normalized wind direction frequencies				
Season	Summer		Winter	
Type	Sea wind	Land wind	Sea wind	Land wind
Frequency	0.4139	0.5861	0.3137	0.6863

Difference of the normalized wind direction frequency between DT and NT (DT-NT)				
Season	Summer		Winter	
Type	Sea wind	Land wind	Sea wind	Land wind
Frequency	0.0731	-0.0731	-0.0697	0.0697

703

704

705

706

707

708

709

710

711

712

713

714

715

716 **Figures**

717



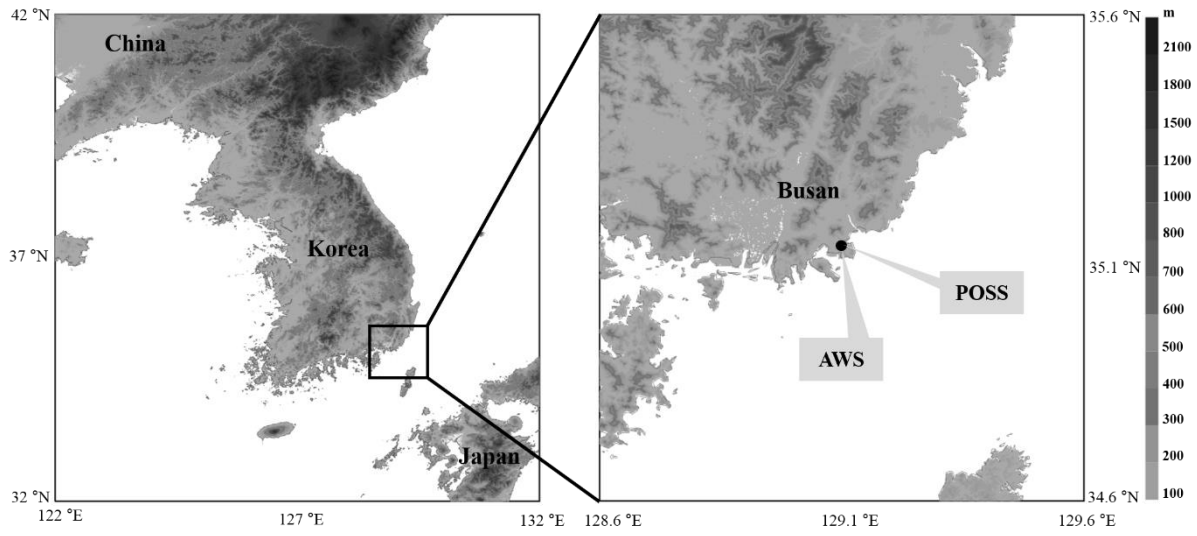
718

719 **Figure 1.**

720 Photograph of the POSS instrument used in this research.

721

722



723

724 **Figure 2.**

725 Locations of the POSS and the AWS rain gauge installed in Busan, Korea.

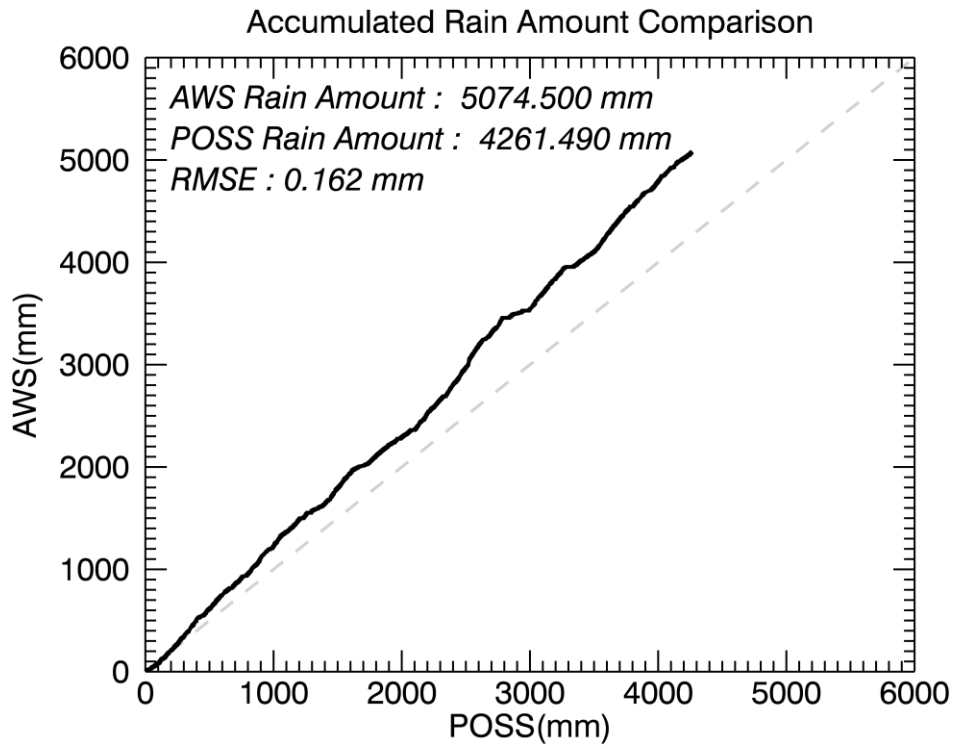
726

727

728

729

730



731

732 **Figure 3.**

733 Comparison of the recorded rainfall amounts between the POSS and AWS instrument.

734

735

736

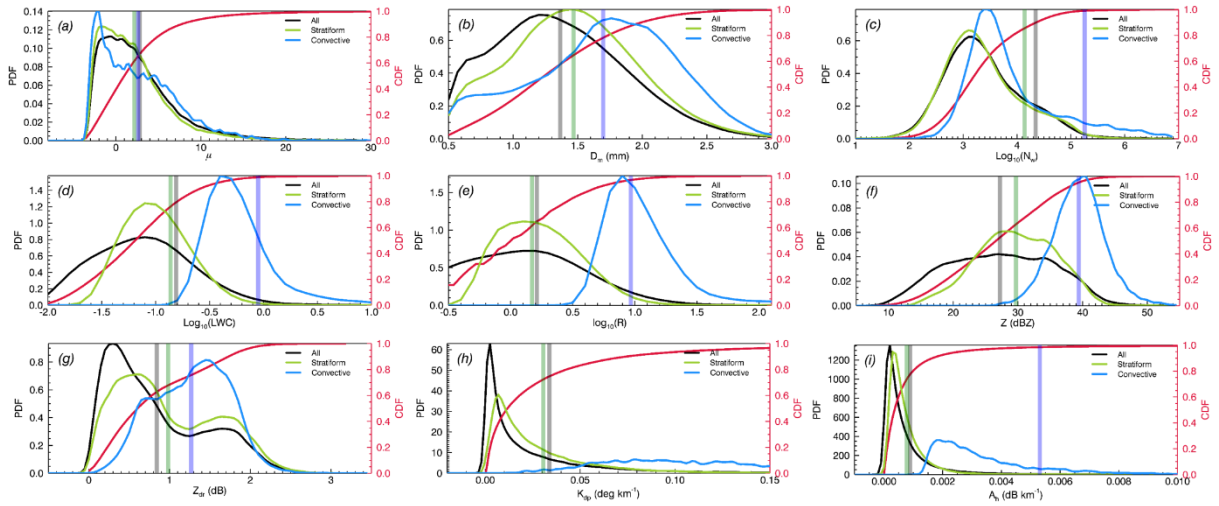
737

738

739

740

741

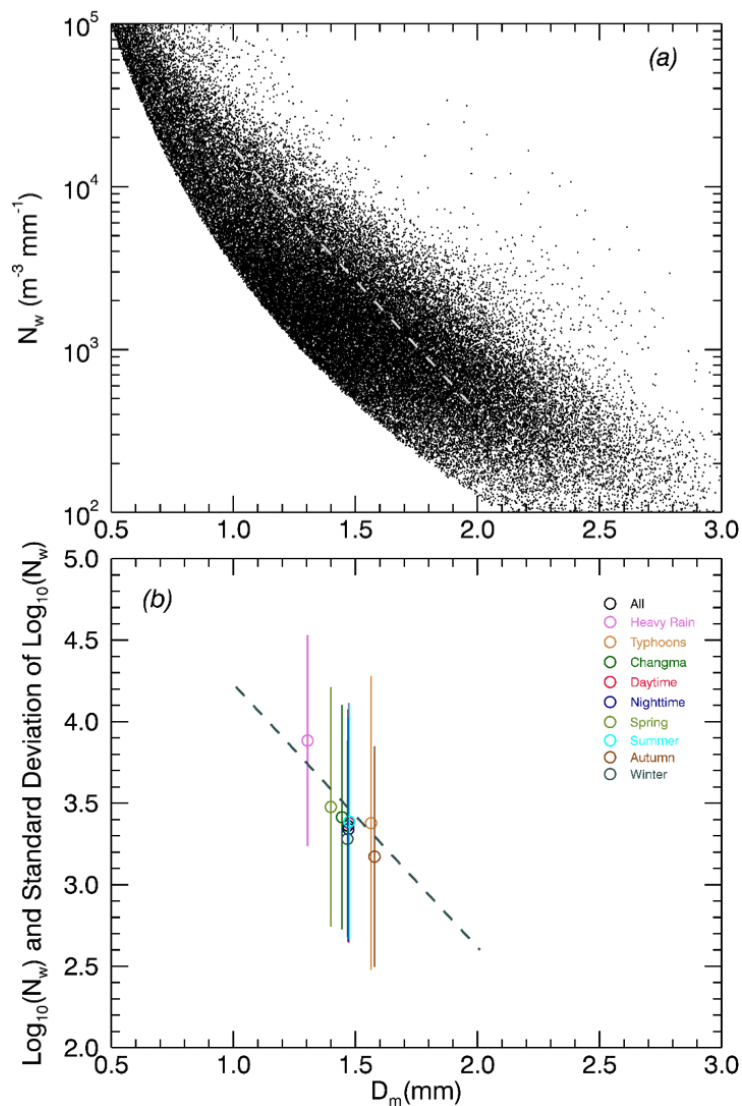


742

743 **Figure 4.**

744 PDF and CDF for (a)  $\mu$ , (b)  $D_m$ , (c)  $\log_{10}(N_w)$ , (d)  $\log_{10}(R)$ , (e)  $\log_{10}(LWC)$ , (f) Z, (g)  
 745  $Z_{dr}$ , (h)  $K_{dp}$ , and (i)  $A_h$  for the entire rainfall dataset (solid black line), stratiform rainfall  
 746 (solid green line), and convective rainfall (solid blue line). The solid red line represents the  
 747 CDF for entire rainfall dataset. The solid vertical line represents the mean value of each type.

748



749

750 **Figure 5.**

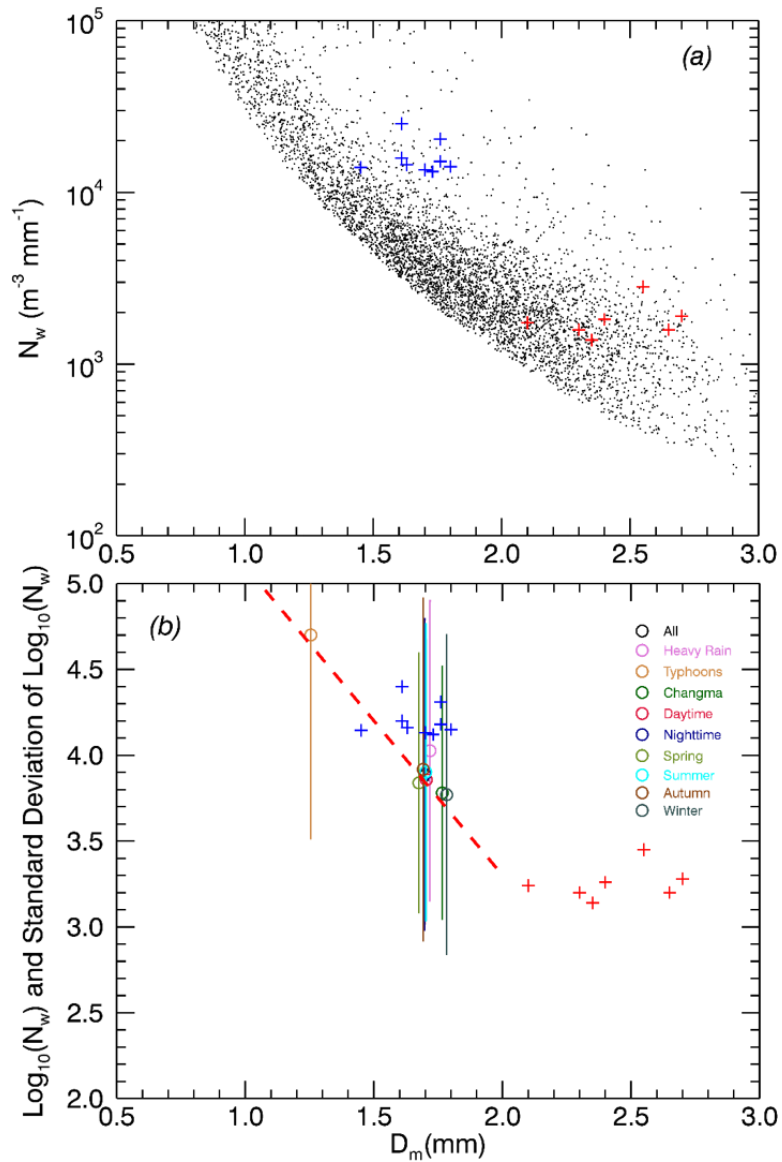
751 (a) Scatter plot of 1-min  $D_m$  and  $N_w$  for the 10 rainfall categories with respect to stratiform

752 rainfall data. The broken grey line represents the average line as defined by Bringi et al. (2003).

753 (b) Scatter plot of mean  $D_m$  and  $\log_{10}(N_w)$  values of the 10 rainfall categories with respect

754 to stratiform rainfall and these mean values for each rainfall type are shown as circle symbols.

755 The vertical line represents  $\pm 1\sigma$  of  $\log_{10}(N_w)$  for each category.



756

757 **Figure 6.**

758 (a) As in Figure 5(a), but for convective rainfall. The blue and red plus symbols represent

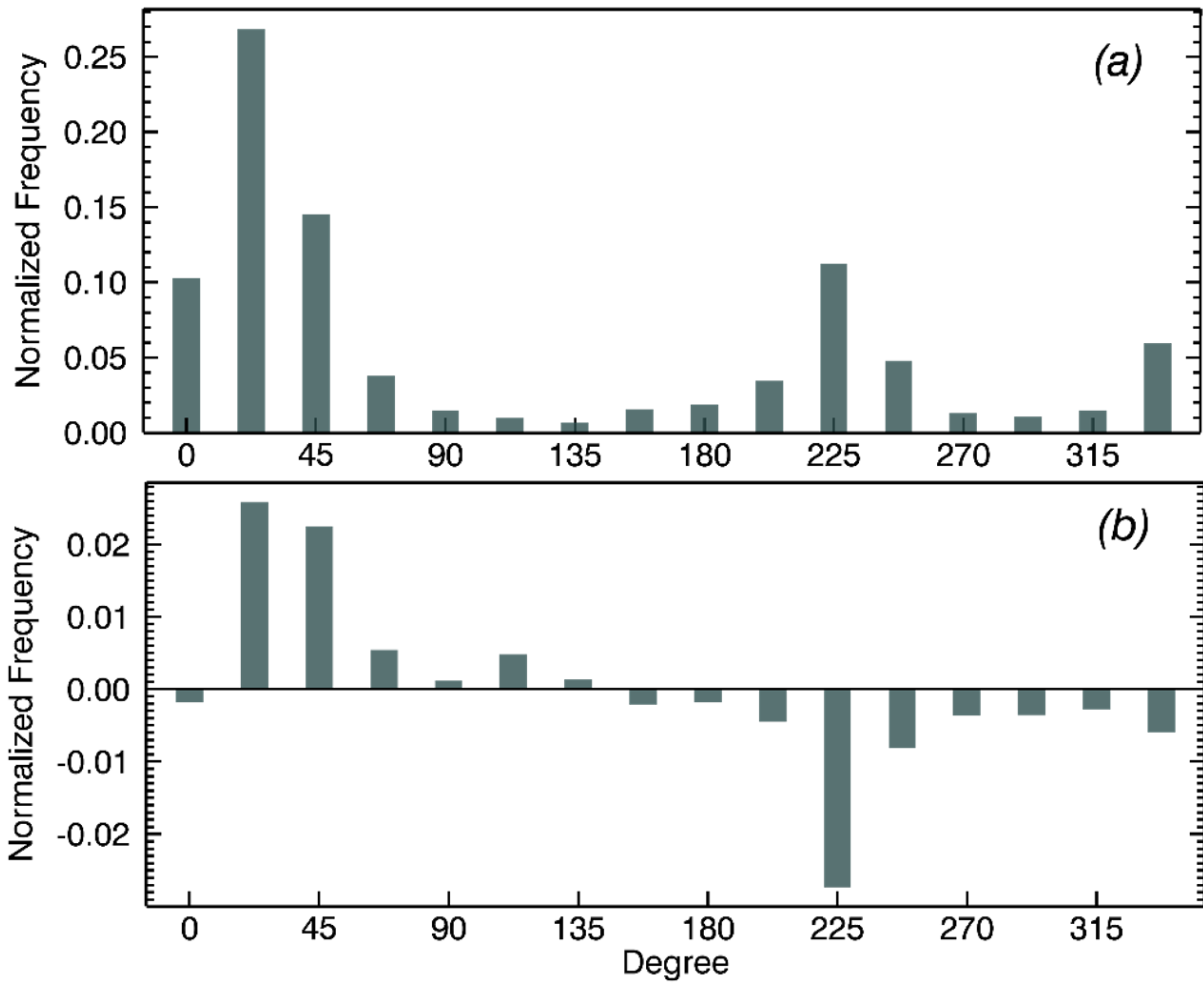
759 maritime and continental rainfall, respectively, as defined by Bringi et al. (2003). (b) As in

760 Figure 5(b), but for convective rainfall. The broken red line represents the mathematical

761 expression described in Eq. (16).

762

763



764

765 **Figure 7.**

766 (a) Histogram of normalized frequency of 16 wind directions for the entire study period. (b)

767 Difference values of wind direction frequencies between DT and NT (DT - NT).

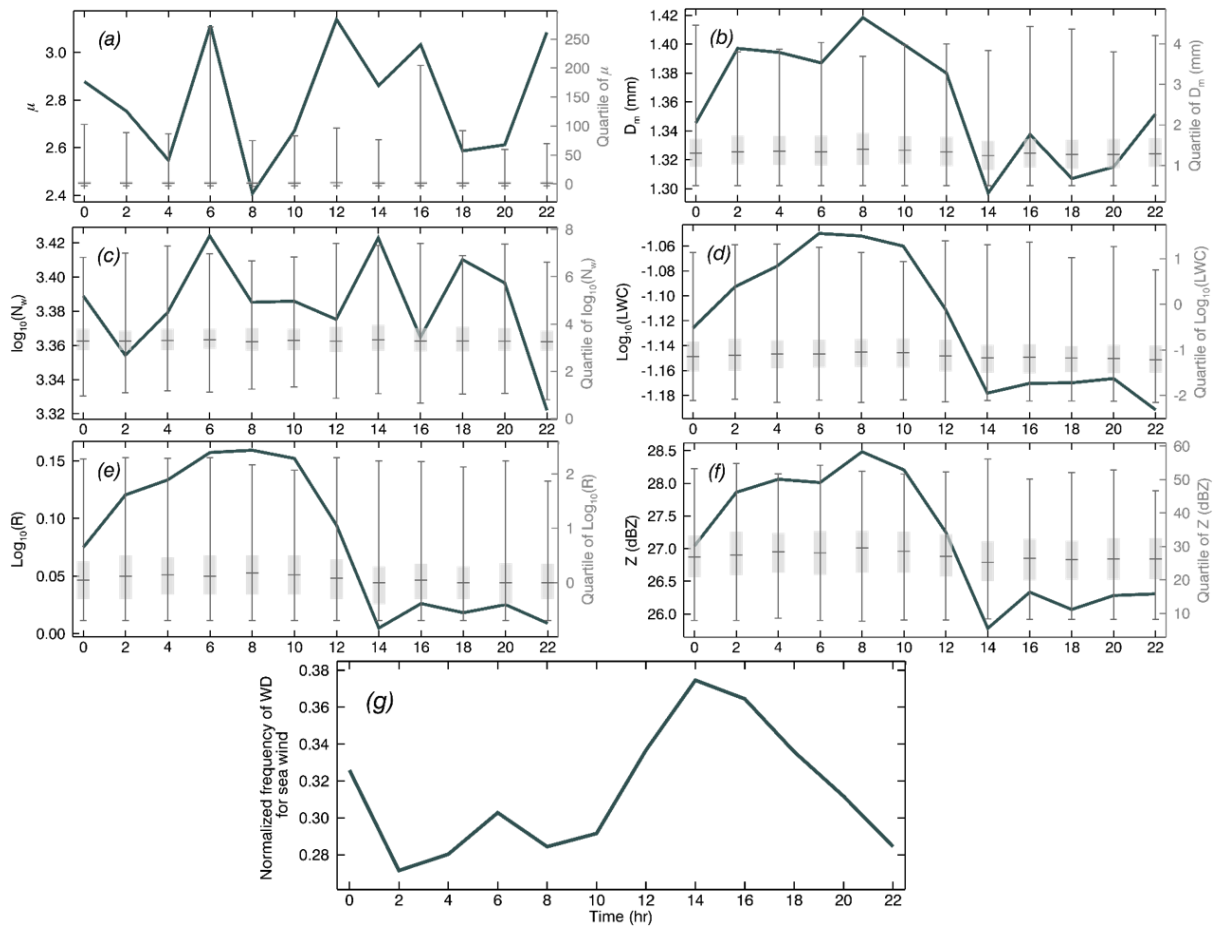
768

769

770

771

772



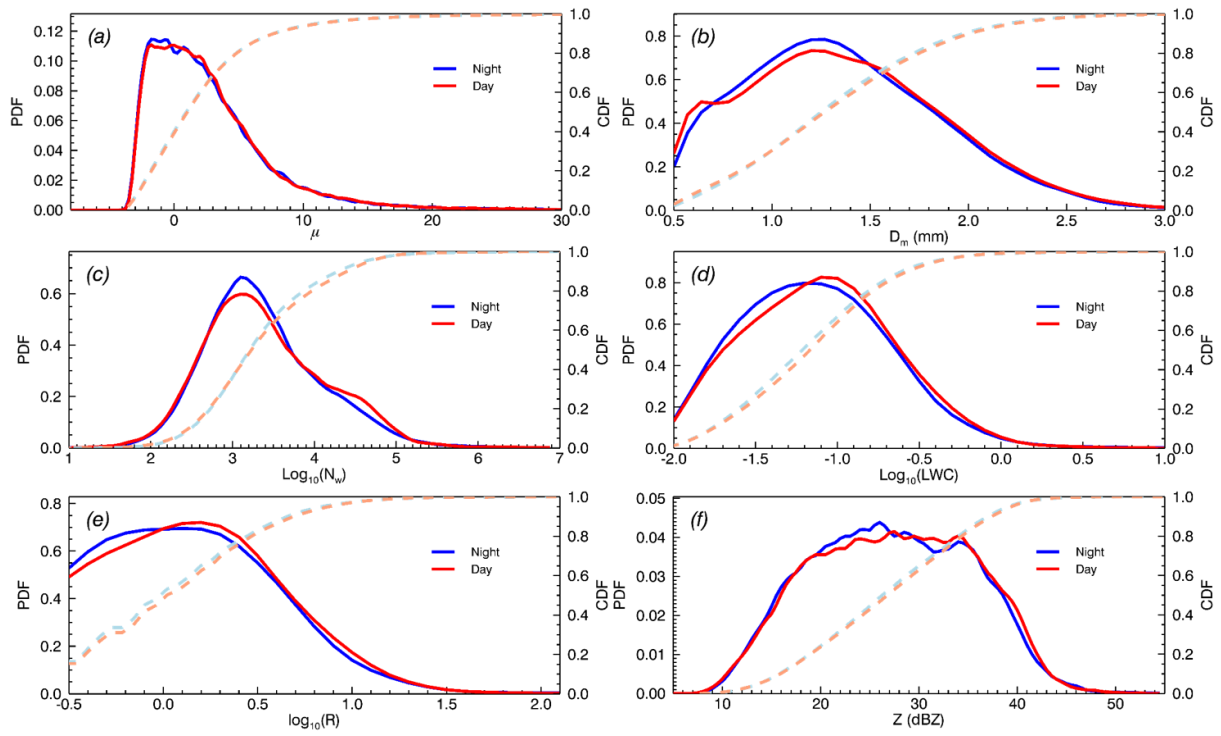
773

774 **Figure 8.**

775 Two hour interval time series of (a)  $\mu$ , (b)  $D_m$ , (c)  $\log_{10}(N_w)$ , (d)  $\log_{10}(R)$ , (e)  
 776  $\log_{10}(LWC)$ , (f)  $Z_h$  and (g) normalized frequency of wind direction for sea wind ( $45^\circ$  to  $225^\circ$ )  
 777 with quartiles for the total period. Solid lines are quartiles for each time.

778

779



780

781 **Figure 9.**

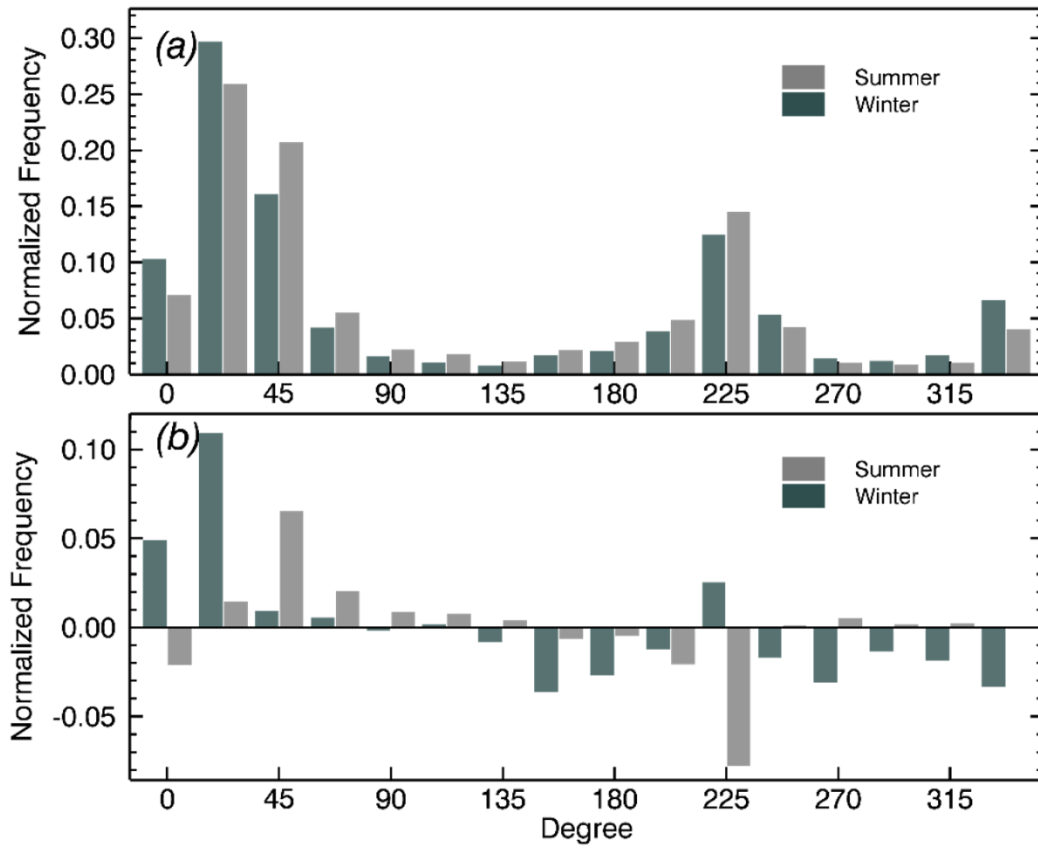
782 PDF and CDF curves for (a)  $\mu$ , (b)  $D_m$ , (c)  $\log_{10}(N_w)$ , (d)  $\log_{10}(R)$ , (e)  $\log_{10}(LWC)$ , and  
 783 (f)  $Z$  for DT and NT according to the entire period. The solid red and blue lines represent the  
 784 PDF for DT and NT, respectively. The broken light red and blue lines represent the CDF for  
 785 DT and NT, respectively.

786

787

788

789



790

791 **Figure 10.**

792 Histogram of normalized frequency for 16 wind directions in (a) the entire period and (b)  
 793 differences of normalized frequency with respect to wind directions between DT and NT (DT  
 794 - NT) for Summer (light grey) and Winter (dark grey) season.

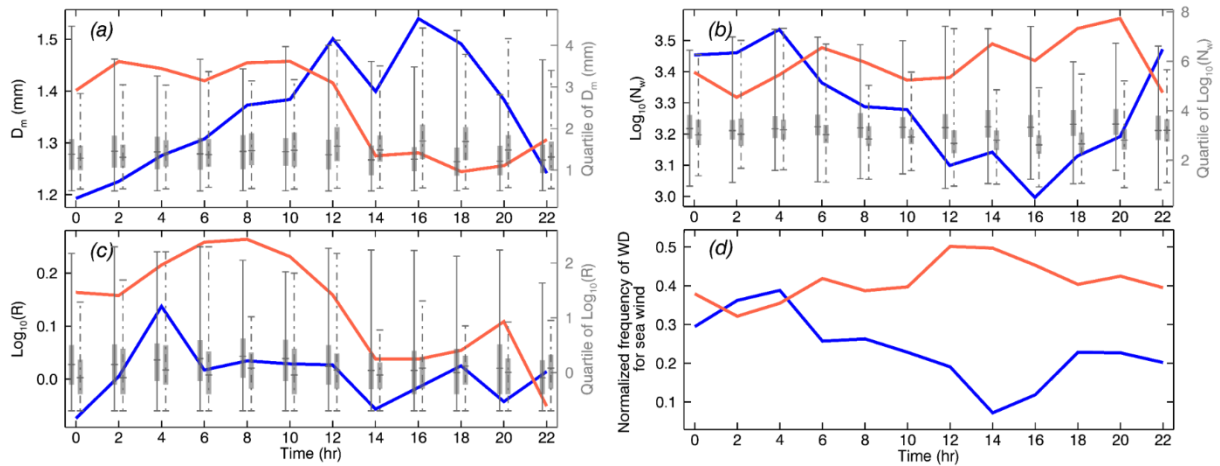
795

796

797

798

799



800

801 **Figure 11.**

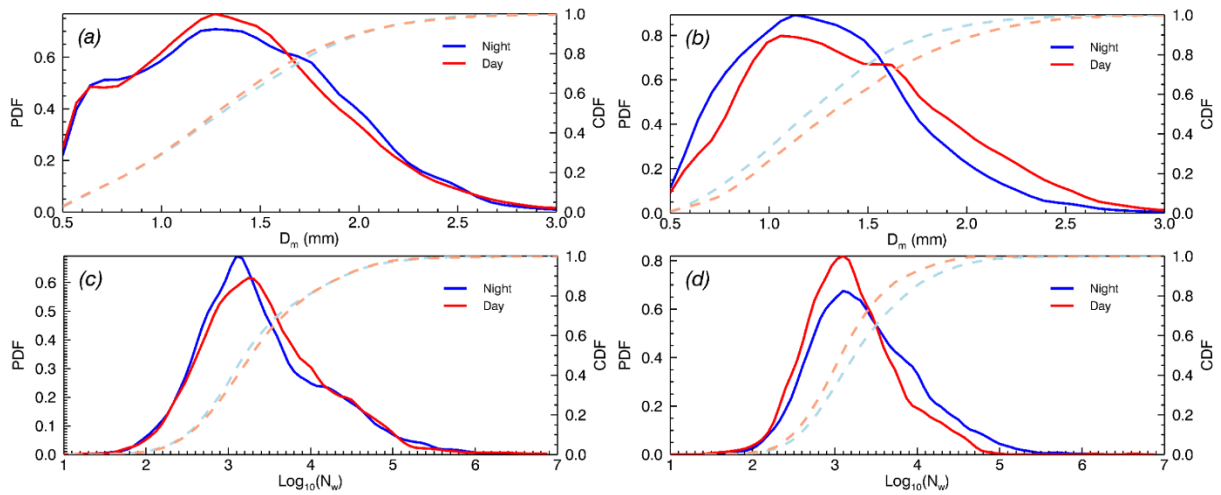
802 Two hour interval time series and quartiles of (a)  $D_m$ , (b)  $\log_{10}(N_w)$  (c)  $\log_{10}(R)$  and (d)  
 803 normalized frequency of wind direction for sea wind ( $45^\circ$  to  $225^\circ$ ) for the Summer (red) and  
 804 Winter (blue) season. Solid (broken) lines are quartiles of Summer (Winter) for each time,  
 805 respectively.

806

807

808

809



810

811 **Figure 12.**

812 PDF and CDF of (a)  $D_m$  ((b)  $D_m$ ) and (c)  $N_w$  ((d)  $N_w$ ) for the entire rainfall type in the

813 Summer (Winter) season. Red and blue solid lines represent the PDF of DT and NT,

814 respectively. The light red and blue broken lines represent the CDF for each season

815

816

817

818

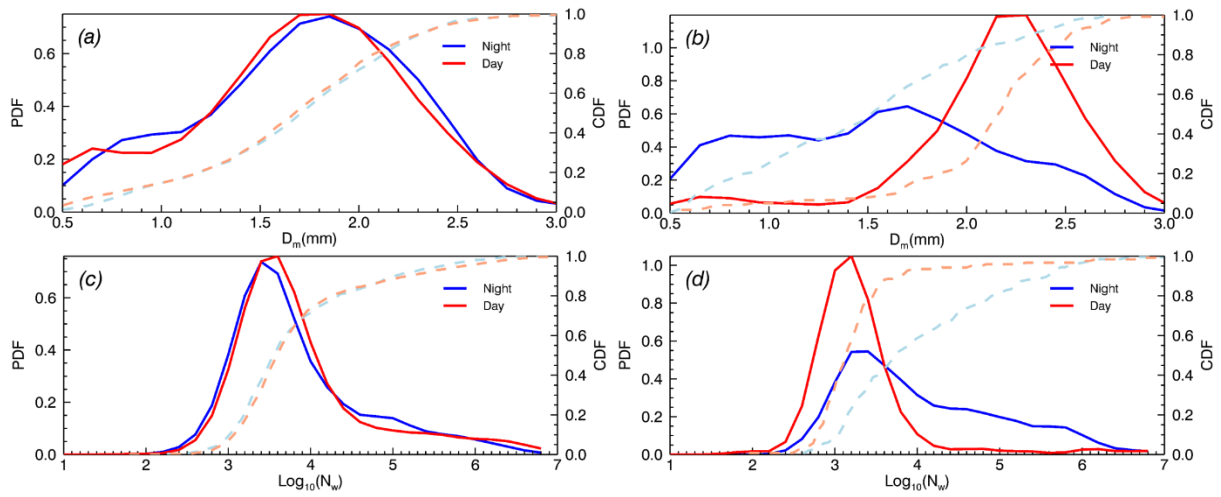
819

820

821

822

823



824

825 **Figure 13.**

826 As in Figure 12, but for convective rainfall type.

827

828

829

830

831

832

833